Range Error Detection and Evaluation for retroreflective Road Signs in Phase-Shift MMS Point Clouds

Saori Fukushi [1], Yoji Takahashi[2], Hirofumi Chikatsu[3]

[1] Aero Toyota Co., Ltd., System Development Division, Japan – saori-fukushi@aerotoyota.co.jp
[2] Aero Toyota Co., Ltd., Technology Division, Japan – youji-takahashi@aerotoyota.co.jp
[3] Tokyo Denki Uni., Japan – chikatsu@g.dendai.ac.jp

Keywords: Mobile Mapping System, Phase-Shift LiDAR, Point Cloud, Range error, Ghost Point Detection, Retroreflective Material.

Abstract

In this study, we addressed the problem of range errors in point clouds of road signs acquired using a mobile mapping system (MMS) equipped with a phase-shift laser scanner. Under certain conditions, retroreflective materials used for road signs cause points to be output at locations different from their true positions. Although previous studies have developed techniques to reduce range errors of time-of-flight scanners, similar research on phase-shift scanners is scarce. Furthermore, many existing approaches for detecting road signs from point clouds assume that sufficient points on the sign surface are captured. Therefore, they are inapplicable when range errors affect numerous sign points. Against this background, first, we located road signs by converting the point clouds into images and identifying the signs in the image domain. We then developed a method to determine the presence of range errors based on the standard deviation of the relative distances from a reference emission point. To validate the developed method, we used 5 km of driving data collected from general roads. Consequently, 32 road signs were extracted, of which 26 were detected as exhibiting range errors in agreement with visual assessment. These findings show the effectiveness of the developed detection method and highlight its potential for improving the reliability of identifying range error-affected road signs on general roads.

1. Introduction

In recent years, efforts to utilize three-dimensional information about road environments for purposes such as improving the efficiency of maintaining aging transportation infrastructure and constructing digital twins of urban spaces have been increasing. A mobile mapping system (MMS) is one of the most widely used methods to accurately measure road environments. Point cloud data acquired by an MMS serve as essential inputs for various downstream processes, including recognition of roadside objects, automated detection of structural defects, and artificial intelligence-based classification. Therefore, the quality of point clouds significantly affects the subsequent processing, and noise can cause errors in shape estimation and decrease the processing accuracy.

Recently, MMSs equipped with phase-shift laser scanners, which offer higher ranging accuracy than time-of-flight (TOF) scanners, have become available. However, when measuring objects with high reflectivity, such as road signs, phase-shift scanners may produce range errors, which cause ghost points to be generated behind an object along the laser emission direction (Sasano et al., 2022; Kato et al., 2023). An example of a road sign affected by range errors is shown in Figure 1. This point cloud is captured using a laser scanner mounted at a rigging angle of 45°, and layered ghost points are observed behind the true position of the road sign.

According to manufacturer, this phenomenon is a Nonius jump and caused by the retroreflective materials used for road signs. Retroreflective materials are optical components designed to return incident light to the source without attenuation, thereby allowing drivers to recognize road signs. However, because laser scanners are designed assuming diffuse reflection from object surfaces, the extremely strong reflected light from the retroreflective materials of sign boards saturates the receiver and induces a range error.

To address range errors caused by receiver saturation, mitigation and correction methods have been developed for TOF scanners (He et al., 2018). However, very few studies have examined this issue for phase-shift scanners and manufacturers have not disclosed any method to prevent their occurrence.

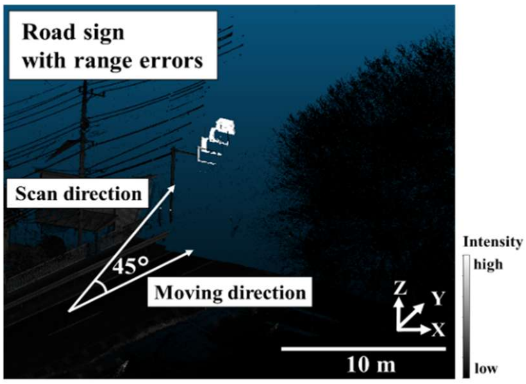

Figure 2. Nonius jumps

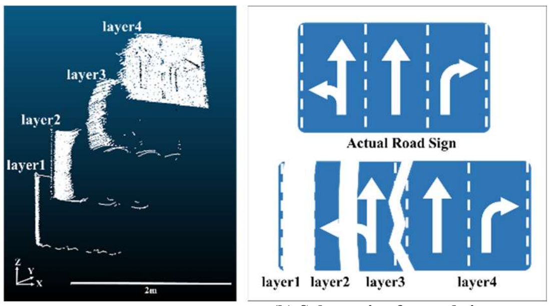

(a) Point cloud of a road sign affected by range errors **(b) Schematic of a road sign with range errors**

Figure 1. Close up of the point cloud of a road sign

Furthermore, many existing studies on road sign detection assume that point clouds representing the sign surface are sufficiently captured. By contrast, point clouds, which were targeted in this study, are often split into multiple layers owing to range errors, as shown in Figure 2(a). Figure 2(a) shows an enlarged view of Figure 1, and Figure 2(b) is a schematic of this phenomenon. When a point cloud deviates significantly from the true sign locations, existing detection methods become difficult to be used.

Because of these problems, field operators must visually confirm the locations of road signs and manually remove ghost points for signs affected by Nonius jumps, which results in a substantial workload.

To address this problem, we developed a method that extracts road signs via point-cloud image conversion and detects range errors using the standard deviation of the relative distances (Fukushi et al., 2025).

In this study, we applied the developed method to 5 km of MMS driving data collected on general roads. General roads have more complex surroundings than highways, which were used in earlier studies. We also validated it by comparing the results with visual assessments.

2. Methodology

The process flow of the developed method is shown in Figure 3. The method consists of two components: a road sign extraction algorithm based on point-cloud image conversion and a range error detection algorithm that uses the standard deviation of the relative distances from a reference emission point.

The specifications and measurement parameters of the equipment used in this study are listed in Table 1.

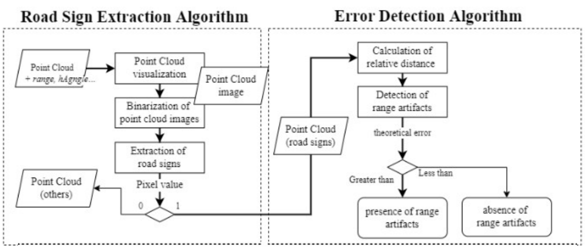

Figure 3. Overview of the processing pipeline

Parameter	Value
Sensor Type	Z+F Profiler 9012
Distance Accuracy (≤50 m)	0.2–0.98 mm
Measurement Range	0.3–119 m
Scan Rate	1 million points/s
Vertical Field of View	360°
Rotation Speed	200 Hz
Mounting Angle	45°
GNSS/IMU Horizontal Accuracy	0.02–0.05 m

Table 1. Measurement specifications

We used an MMS equipped with a phase-shift two-dimensional (2D) laser scanner for the measurements. As shown in Figure 4, the scanner acquires point clouds around a roadway by performing a helical scan while driving. During the measurement, the laser emission direction and rotation count of the scanner are recorded.

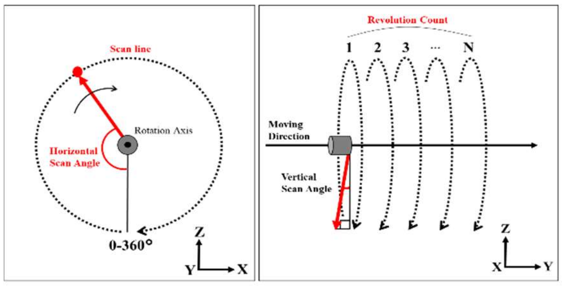

Figure 4. Measurement concept of the 2D laser

2.1 Point-Cloud Image Conversion

For a road sign affected by range errors, layered ghost points appear behind the sign surface, which makes it difficult to identify the road sign in three-dimensional space. Therefore, following a previous study (Vallet et al., 2015; Takahashi et al., 2019), we converted each point cloud into an image and identified road-sign points based on point continuity and reflection intensity.

As shown in Figure 5, a point cloud is rearranged into an image, with the vertical and horizontal axes representing the rotation count of the laser scanner and horizontal emission angle, respectively. To place road signs directly above the driving lane at the center of the image, the horizontal center is set at 180°. The pixel values are scaled to 0–255 based on the reflection intensity. In Figure 5, regions without returns, such as the sky, are shown in blue.

Furthermore, Sasano et al. (2022) reported that Nonius jumps occur when the incident angle between the target and laser beam is 68° or less. Based on this finding, in this study, image generation was limited to regions where the incident angle to the road signs installed above the driving lane was 70° or less.

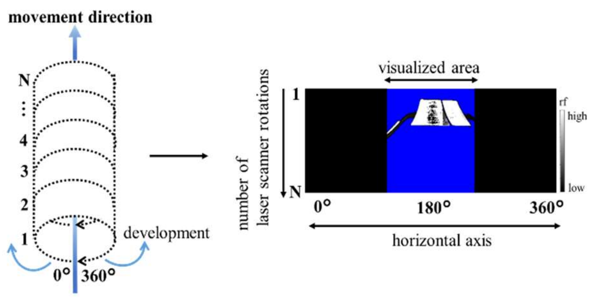

Figure5. Point-cloud image conversion

2.2 Binarization of a Point-Cloud Image

Figure 6 shows examples of the reflection intensity outputs for several objects. The receiver had a hardware-dependent measurable intensity range (scanner range), and any reflection intensity exceeding the upper limit was clipped. The retroreflective materials used for road signs exhibit reflectance values that are up to 1000 times higher than those of standard reference plates (Dickerson et al., 1991; Halstuch and Yitzhaky, 2008). Therefore, the reflection intensities returned from the road signs exceeded the scanner range and were recorded as clipped upper-limit values.

Thus, in the point-cloud images generated for this study, pixels with values of 255 corresponded to objects that returned reflections that were sufficiently strong to saturate the receiver. Based on this characteristic, a threshold of 254 was applied for binarization. An example binarized image is shown in Figure 7

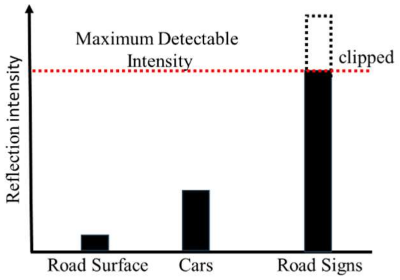

Figure6. Reflection intensity and scanner range

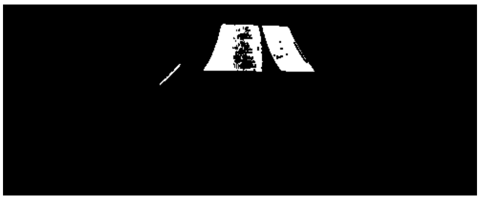

Figure 7. Example binarized point-cloud image

2.3 Extraction of Road-Sign Point Clouds

The point clouds corresponding to each road sign were extracted. Each sign was identified by applying contour extraction to the binarized image. As described in Section 2.1, point-cloud images were constructed using the rotation count of the laser scanner and horizontal emission angle as the vertical and horizontal axes, respectively. Thus, the corresponding rotation count and emission angle could be reconstructed from the row and column indices of the detected road-sign pixels.

In some cases, black pixels appeared within the white regions of the binarized images (where the pixel value was one). These black pixels were probably caused by the receiver becoming saturated, which resulted in range errors and abnormally low reflection-intensity values. To address this issue, as shown in Figure 8, we search each row independently and determine the minimum and maximum column indices of the white pixels. All points within this range are then treated as part of the road sign, and the corresponding point clouds are extracted accordingly.

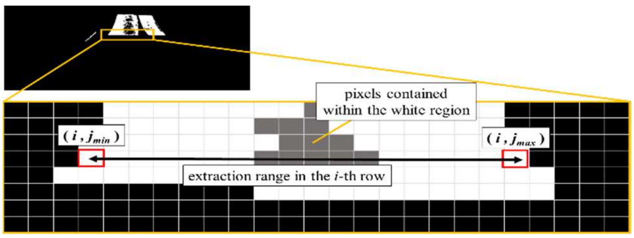

Figure 8. Searching for point clouds constituting a road sign

2.4 Calculation of Relative Distances from the Reference Point

In this section, we present the definition and calculation method for the relative distances used to evaluate the variation in the point clouds. These constitute a preliminary step for detecting range errors in the road signs extracted, as described in Section 2.3. Because range errors cause point clouds to be output behind the true positions of a road sign, the presence of range errors can be determined by evaluating the variation in the point clouds in the driving direction for each extracted road sign. However, because the MMS acquired measurements while moving, evaluating the variation in the point clouds in the driving direction using only the local coordinate system was difficult.

Therefore, in this study, as shown in Figure 9, the farthest emission point from which road sign returns are observed is defined as the reference emission point.

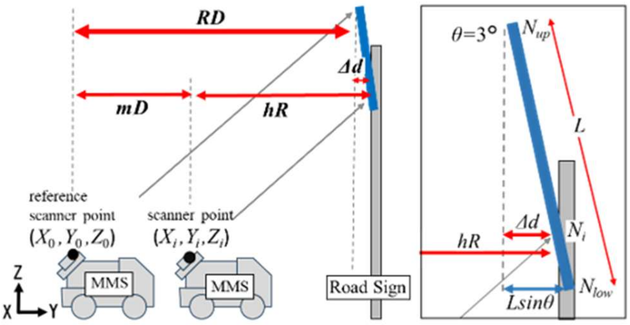

Figure 9. Relative distances between the MMS

Equation (1) was used to calculate the relative distances of all points extracted as the road sign. The right-hand terms in Equation (1) correspond to Equations (2)–(4).

$$\boldsymbol{RD = mD + hR - \Delta d} \tag{1}$$

where RD = relative distance,
mD = movement distance,
hR = horizontal range, and
Δd = depth distance caused by sign tilt.

$$\boldsymbol{mD = \sqrt{(X_i - X_0)^2 + (Y_i - Y_0)^2}} \tag{2}$$

where X_i, Y_i = horizontal coordinates of the scanner point and X_0, Y_0= horizontal coordinates of the reference scanner point.

$$\boldsymbol{hR = range * \cos(hAngle - 180) * \cos(vAngle + rAngle)} \tag{3}$$

where $range$ = measurement range,
$hAngle$ = horizontal field of view (HFOV),
$vAngle$ = vertical field of view (VFOV), and
$rAngle$ = rigging angle.

$$\boldsymbol{\Delta d = L * sin(\theta) * \frac{(N_i - N_{up})}{(N_{low} - N_{up})}} \tag{4}$$

where L = vertical dimension of the road sign,
θ = installation angle of the road sign (3° in this study), and
N = number of laser scanner rotations.

In Equation (4), the vertical dimension L of the road sign is obtained using Equation (5). It is based on P_{up}, the point with the smallest Z-coordinate in the point-cloud image, and P_{low}, the point with the smallest Z-coordinate among the points identified as the lower edge of the road sign, as shown in Figure 10.

$$\boldsymbol{L = \sqrt{(Z_{up} - Z_{low})^2 + (Y_{up} - Y_{low})^2}} \tag{5}$$

where (Y_{up}, Z_{up}) = coordinates of point P_{up} and
(Y_{low}, Z_{low}) = coordinates of point P_{low}.

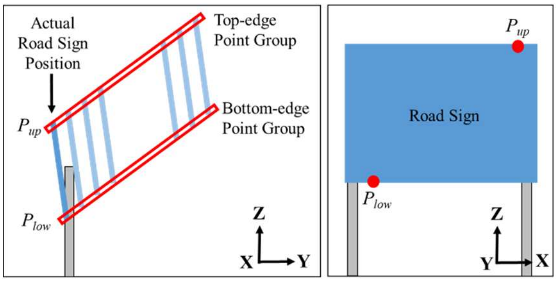

Figure 10. Estimation of the vertical dimension of a road sign

2.5 Detection of Range Errors

Finally, the range errors were detected based on the variation in the relative distances computed for each road sign, as outlined in Section 2.4. Figure 11(a) and (b) show histograms of the relative distances for a normally measured sign without range errors and sign affected by range errors, respectively. The relative distances in Figure 11(a) follow a normal distribution, whereas multiple peaks appear in Figure 11(b) because the point clouds are output behind the actual sign owing to range errors. This suggests that the variation (standard deviation) in the relative distances differs significantly depending on occurrence of range errors.

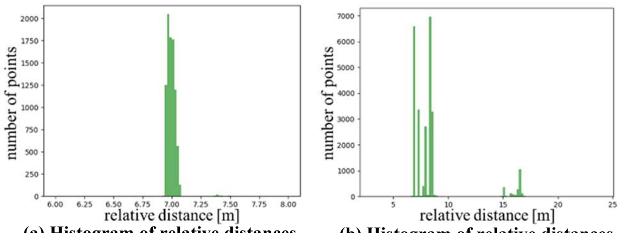

Figure 11. Histograms of relative distances

Therefore, in this study, the theoretical error of the relative distance was obtained by applying the law of error propagation to Equation (1). This value was then used as the threshold for detecting road signs affected by range errors.

Equation (6) expresses the standard deviation of the relative distances derived by applying error propagation to Equation (1).

$$\sigma_{RD} = \sqrt{\left(\frac{\partial RD}{\partial mD}\right)^2 \sigma_{mD}{}^2 + \left(\frac{\partial RD}{\partial hR}\right)^2 \sigma_{hR}{}^2 + \left(\frac{\partial RD}{\partial \Delta d}\right)^2 \sigma_{\Delta d}{}^2} \tag{6}$$

where $\sigma_{mD}{}^2$ = variance of the movement distance,
$\sigma_{hR}{}^2$ = variance of the horizontal range from the emission point to the road sign, and
$\sigma_{\Delta d}{}^2$ = variance of the depth distance caused by the tilt of the road sign.

Here, $\sigma_{hR}{}^2$ denotes the variance of the horizontal range from the emission point to the road sign. By applying the law of error propagation to Equation (3), $\sigma_{hR}{}^2$ is expressed in terms of the propagated variances of *range*, *hAngle*, and *vAngle*. These variances are sufficiently small compared to the horizontal accuracy of the GNSS/IMU (refer to Table 1), and therefore, can be neglected. Similarly, $\sigma_{\Delta d}{}^2$ represents the variance of the depth distance caused by the tilt of the road sign. Because the installation angle in Equation (4) is as small as 3°, its contribution is also negligible. Thus, the variation in the relative distance σ_{RD} is considered to be affected only by σ_{mD}.

Equation (7) is derived by applying the law of error propagation to Equation (2), which is the formula for computing mD. In this derivation, the variances in the planar coordinates of the reference and emission points during vehicle movement are assumed to correspond to the horizontal accuracy of the GNSS/IMU mounted on the MMS. Assuming that the horizontal accuracies in the X and Y directions during measurement are equal, the equation can be expressed as Equation (8).

$$\sigma_{mD} = \sqrt{\left(\frac{\partial mD}{\partial X_i}\right)^2 \sigma_{X_i}{}^2 + \left(\frac{\partial mD}{\partial Y_i}\right)^2 \sigma_{Y_i}{}^2 + \left(\frac{\partial mD}{\partial X_0}\right)^2 \sigma_{X_0}{}^2 + \left(\frac{\partial mD}{\partial Y_0}\right)^2 \sigma_{Y_0}{}^2} \tag{7}$$

where $(\sigma_{X_0}{}^2, \sigma_{Y_0}{}^2)$ = variance of the planar coordinates of the reference point and
$(\sigma_{X_i}{}^2, \sigma_{Y_i}{}^2)$ = variance of the planar coordinates of the emission point.

$$\sigma_{RD} = \sigma_{mD} = \sqrt{2}\sigma \tag{8}$$

where σ = horizontal accuracy of the GNSS/IMU.

According to Table 1, the horizontal accuracy of the GNSS/IMU used in this study is 0.02–0.05 m. Considering that GNSS/IMU accuracy deteriorates in urban areas, we substituted the upper bound of 0.05 m into Equation (8). Consequently, the theoretical error of the relative distance was calculated to be 0.07 m.

This value was based on the specifications of the equipment used in this study. When applying this method to different MMS platforms, the theoretical errors should be recalculated accordingly.

3. Results

In this chapter, we discuss the results of the evaluation of the developed method in two stages: road sign extraction and range error detection algorithms. The verification was conducted using a 5-km road section, which is shown in Figure 12. As shown in Figure 13, the target area is a major suburban arterial road with two lanes in each direction, where various types of road signs, such as guide and regulatory signs, are installed.

Figure 12. Study area overlaid on GSI Tiles (Geospatial Information Authority of Japan).

Figure 13. Field photographs of the study area

3.1 Road Sign Extraction Results

Figure 14(a) shows an example point-cloud image generated from the MMS data, and Figure 14(b) shows the corresponding binarized image. Figure 15 shows an enlarged view of the area outlined in Figure 14(b). A road sign affected by range errors is present in this area. Although the point clouds of the sign are separated into multiple layers in three-dimensional space owing to range errors, the point-cloud image represents them as a continuous white region. Because the MMS point clouds are dense and large, point-cloud image conversion is performed in segments of several hundred meters.

Table 2 lists the extraction results for the road signs. Of the 33 road signs within the image-converted sections, 32 are extracted by the developed method. A visual inspection of these results confirmed one false positive (FP) case, where a single road sign was mistakenly divided into two, and two false negative (FN) cases, where existing road signs were not detected. No objects other than road signs were erroneously extracted.

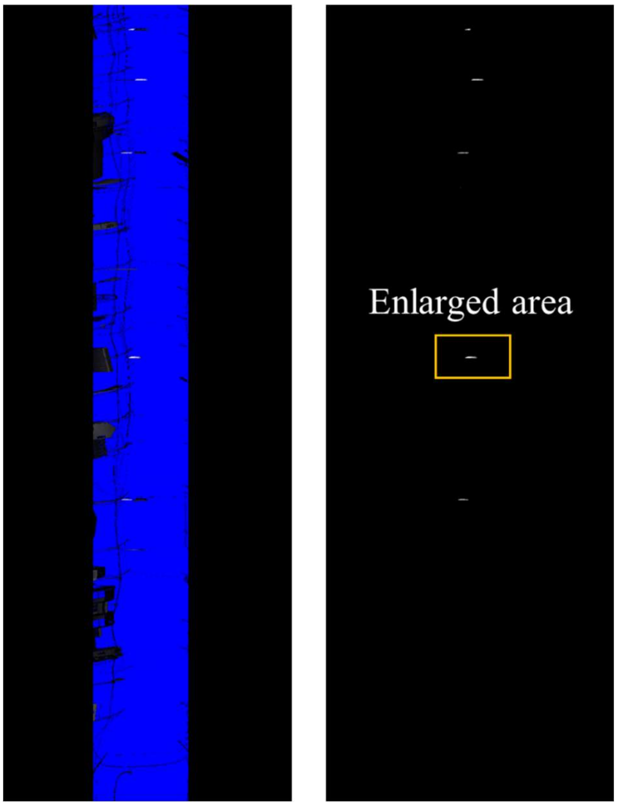

(a) Point-cloud image (b) Binarized image

Figure 14. Point-cloud

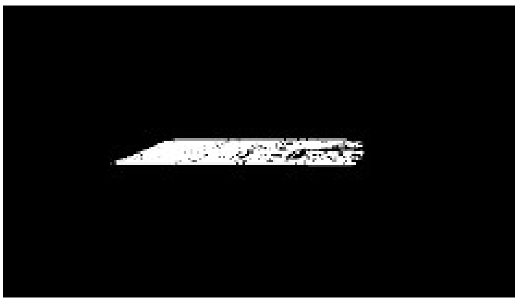

Figure 15. Enlarged view of the binarized image in Figure 14

Number of detections	32
Total number of actual signs	33
True Positive (TP)	31
False Positive (FP)	1
False Negative (FN)	2
Precision	0.969
Recall	0.939
F1-score	0.954

Table 2. Road sign detection results

To evaluate the extraction performance, precision, which is an indicator of the rarity of false detections, was first calculated. Using true positive (TP) = 31 and FP = 1 in Equation (9), precision is 0.969.

$$\mathbf{Precision} = \frac{\boldsymbol{TP}}{\boldsymbol{TP} + \boldsymbol{FP}} \quad \mathbf{(9)}$$

where TP = true positive and
FP = false positive.

Recall, which is an indicator of low occurrence of omissions, was calculated. Using TP = 31 and FN = 2 in Equation (10), recall is 0.939.

$$\mathbf{Recall} = \frac{\boldsymbol{TP}}{\boldsymbol{TP} + \boldsymbol{FN}} \quad \mathbf{(10)}$$

where FN = false negative.

Finally, the F1-score, which evaluates the balance between precision and recall, was calculated. Using Equation (11), the resulting F1-score is 0.954, which indicates high extraction performance with respect to both false and missed detections.

$$\mathbf{F1-score} = \frac{\mathbf{2} \times \boldsymbol{Precision} \times \boldsymbol{Recall}}{\boldsymbol{Precision} + \boldsymbol{Recall}} \quad \mathbf{(11)}$$

3.2 Range Error Detection Results

Range error detection was performed for the 32 road signs extracted, by comparing the standard deviation of the relative distances with a theoretical error of 0.07 m. Consequently, 26 signs were classified as having range errors because their standard deviations exceeded the theoretical error, whereas the remaining 6 signs were classified as not having range errors.

A comparison with the visual assessment results showed complete agreement. All 26 signs classified as having range errors were observed to exhibit range error characteristics, and all 6 signs classified as having no range errors were visually confirmed to be correctly measured. Examples of the extracted signs and their corresponding standard deviations are shown in Figure 16.

Among the six signs determined to have no range errors, some exhibited noise patterns similar to those shown in Figure 17. However, visual inspection confirmed that these were not caused by the Nonius jump phenomenon but rather by spot-splitting noise occurring at the object edges. Therefore, these cases were classified as having no error range.

https://doi.org/10.5194/isprs-archives-XLIX-B1-2026-9-2026

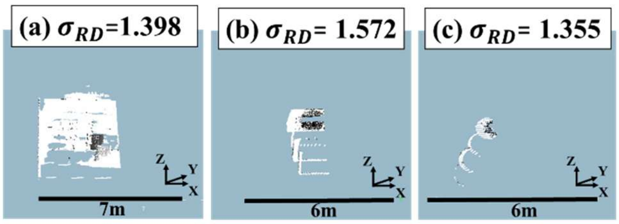

Figure 16. Examples of the range error detection results

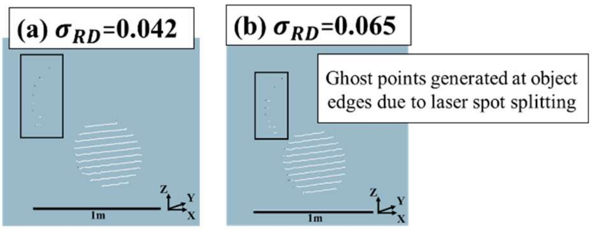

Figure17. Spot-splitting noise at object edges

4. Discussion

The developed method achieved a high extraction accuracy for 5 km of general road data (F1-score = 0.954), which confirmed a favorable balance between false and missed detections in overall road sign extraction. Moreover, the range error detection results agreed 100% with the visual assessment results, which indicated that the decision rule based on the standard deviation of the relative distances was effective even on real-world data. In the following, we discuss the factors affecting FPs and FNs, as reflected in precision and recall, and future directions.

First, precision, which indicates the rarity of false detections, was as high as 0.969. There was only one FP case, in which a single road sign was mistakenly split into two independent signs (Figure 18(a)). As shown in Figure 18(b), a local decrease in the reflection intensity near the center of the sign causes a complete separation of the region in the binarized image, thereby leading to the extraction of separate signs. Briefly, the factor that affected precision was the erroneous splitting caused by a local reduction in reflection intensity.

Regarding recall (0.939), which represents the low occurrence of missed detections (FNs), the road sign for which a missed detection occurred (Figure 19) exhibited the Nonius jump phenomenon, which is known to arise when the receiver becomes saturated. However, the reflection intensity was output at an abnormally low level, and during binarization, the values fell below the threshold, which resulted in the sign region not being extracted. Thus, the factor that affected recall was the failure of region extraction in the image domain caused by abnormal reflection intensity values.

The factor that affected both precision and recall was abnormal reflection intensity. This anomaly caused both erroneous splitting (FP) and missed extraction (FN). The F1-score, which is the harmonic mean of precision and recall, was as high as 0.954. Thus, from the standpoint of balancing false and missed detections, the extraction algorithm maintained a sufficiently high performance.

In addition, for each road sign, the standard deviation of the relative distances from the reference emission point was computed. The results obtained by comparison against the theoretical error were in complete agreement with the visual assessment results. This verified the validity of determining the

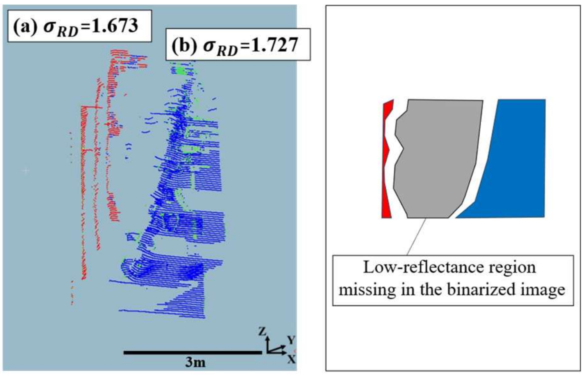

(a) Point cloud view **(b) Illustration of the corresponding scene**

Figure18. Example of a false detection

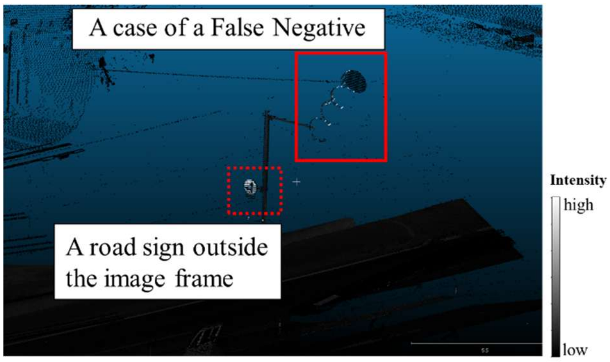

Figure19. Example of a missed detection

presence of range errors based on variations in the point clouds in the driving direction. Furthermore, even when a single road sign was erroneously split, each segment was correctly determined with respect to range error occurrence, which confirmed the robustness against erroneous splitting of the same sign.

In summary, the findings confirm that even under real-world conditions, the range error detection algorithm exhibits high decision accuracy for extracted road signs. However, issues remain in the extraction of road signs due to abnormal reflection intensity values, and we plan to improve the extraction method in a future study.

5. Conclusion

In this study, we validated a road sign extraction algorithm based on point-cloud image conversion and a range error detection method based on the standard deviation of relative distances. We used 5 km of point-cloud data acquired on general roads using an MMS equipped with a phase-shift laser scanner.

The extraction accuracy achieved precision of 0.969, recall of 0.939, and F1-score of 0.954, which exhibit high performance with respect to both false and missed detections. Moreover, the range error detection results matched the visual assessment results with complete (100%) consistency, thereby confirming that the decision method based on the standard deviation of relative distances is effective even when applied to real-world data.

Acknowledgements

We would like to express our sincere gratitude to Mr. Iwakami of Nikon-Trimble for providing valuable information on the Nonius jump phenomenon during the course of this study.

References

Dickerson, SL., Lee, K., Lee, E., Single, T., Li, D.,1991: Intelligent material handling：use of vision. *Intelligent robots and computer vision IX : algorithms and techniques*, Vol.1381, 201-209.

Fukushi, S., Takahashi, Y., Chikatsu, H., 2025: Road signs detection and evaluation of distance measurement errors observed in MMS point clouds equipped with phase-shift laser scanners. *Journal of the Japan Society of Photogrammetry and Remote Sensing*, 64(3), 94-99.

Halstuch, A., Yitzhaky, Y., 2008: Properties of light reflected from road signs in active imaging, *Applied Optics*, 47(22), 4031-4036.

He, W., Sima, B., Chen, Y., Dai, H., Chen, Q., Gu, G., 2013:A correction method for range walk error in photon counting 3D imaging LIDAR. *Opt. Commun*, 308(11), 211−217.

Kato, S., Yamaguchi, Y., Okamoto, N., Iwakami, H, Sada, T., Emori, H., 2023: Study on Material Conditions and Incident Angle that Generate Noise During Measurement with MMS Equipped with Phase-Shift Laser Scanner. *Journal of applied survey technology*, 34,109-119.

Sasano, T., Yamaguchi, Y., Shiraishi, S., Okamoto, N., Iwakami, H., Sada, T., 2022: AN INSPECTION OF PROPERTIES EQUIP MMS WITH PHASE DIFFERENTIAL LASERSCANNER MEASUREMENT MATERIAL TYPES. *Journal of Japan Society of Civil Engineers, Ser. F3, Civil Engineering Informatics,* 78(2), II.26-II.33.

Takahashi, G., Masuda, H., 2019: TRAJECTORY-BASED VISUALIZATION OF MMS POINT CLOUDS. The International Archives of the Photogrammetry, *Remote Sensing and Spatial Information Sciences*, Volume XLII-2/W13, 1127-1133

Vallet, B., Brédif, M., Serna, A., Marcotegui, B., Paparoditis, N., 2015: TerraMobilita/iQmulus Urban Point Cloud Analysis Benchmark. *Computers & Graphics*, 49, 126-133.